Journal of Materials Chemistry A

PAPER

View Article Online
View Journal | View Issue

Cite this: J. Mater. Chem. A, 2019, 7, 24557

Unraveling the Na-ion storage performance of a vertically aligned interlayer-expanded two-dimensional MoS_2@C@MoS_2 heterostructure†

Ganesh Kumar Veerasubramani, [a] Myung-Soo Park,[a] Goli Nagaraju [b] and Dong-Won Kim *[a]

Received 13th August 2019
Accepted 29th September 2019

DOI: 10.1039/c9ta08839c

rsc.li/materials-a

Achieving hierarchically uniform surface manipulated nanostructured materials is important to accomplish high performance storage devices, but it is still challenging. Herein, we successfully synthesized a vertically-aligned interlayer-expanded caterpillar-like heterostructure consisting of MoS_2@C nanosheets (NSs) over MoS_2 nanorods (NRs) (MoS_2@C@MoS_2) as an advanced anode material for sodium-ion batteries (SIBs). Step-wise ramp rate tuned MoS_2 nanorods (NRs) were achieved *via* surface sulfurization of MoO_3 NRs by a vapor phase ion-exchange method. Heterointerphased MoS_2@C nanosheets performed a crucial role in enacting an excellent electrochemical performance by facilitating better Na^+ ion diffusion and faster electron transport. The hierarchical MoS_2@C@MoS_2 electrode delivered a high specific capacity of 434 mA h g^{-1} (after 100 cycles at 100 mA g^{-1}) and excellent cycling stability (352 mA h g^{-1} after 200 cycles at 1000 mA g^{-1}). Kinetic analysis revealed that an enhanced sodium storage performance of the MoS_2@C@MoS_2 electrode could be accompanied by an ameliorated capacitive contribution reaction. Moreover, the sodium-ion full cell assembled with the MoS_2@C@MoS_2 anode and a $Na_3V_2(PO_4)_2F_3$ cathode exhibited a high specific capacity of 320 mA h g^{-1} with good capacity retention.

Introduction

Developing an advanced energy storage device such as lithium-ion batteries (LIBs) for renewable energy resources is of great importance to address the energy crisis facing mankind in recent days.[1,2] Beyond LIBs, sodium-ion batteries (SIBs) stand out as an auspicious choice owing to the outstanding properties of Na metal, such as large abundance (2.36%) and an appropriate redox potential (−2.71 V *vs.* SHE).[3,4] However, the larger ionic radius of Na^+ ions than that of Li^+ ions (0.76 Å) hinders their structural variability and limits their specific capacity in SIBs, which consequently results in poor electrochemical performance.[5] Thus, an advancement of suitable electrode materials for Na^+ ion insertion/extraction and accommodation with an adequate interlayer spacing is necessary.

Recently, nanostructured two dimensional (2D) layered metal dichalcogenides (TMDs) such as MoS_2, $NbSe_2$, SnS_2, WS_2, and VS_2 have attracted great attraction because of their large interlayer spacing that provides a wide range of alternatives for developing superior anodes for SIBs.[6–10] Among the various 2D TMDs, MoS_2 has attracted great attention due to its layered structure analogous to that of graphite, high theoretical capacity (670 mA h g^{-1}), which is two-fold higher than that of commercial graphite, and relatively low cost.[11,12] There are enormous S–Mo–S units in MoS_2 with strong covalent bonds where Mo atoms are congregated at the center which were enclosed by S atoms. Such a high theoretical capacity has been attained by a favorable intercalation reaction ($MoS_2 + xNa \rightarrow Na_xMoS_2$) followed by conversion chemistry ($Na_xMoS_2 + (4 - x)Na \rightarrow Mo + 2Na_2S$, where Na^+ ions react with MoS_2, and MoS_2 is fully converted into Mo metal and Na_2S).[13] However, there are some obstacles for the MoS_2 use in practical applications due to its poor cyclability, inferior rate capability due to its lower electronic conductivity and severe damage of the 2D layered structure during repeated cycling. In addition, although it can achieve high capacity at lower potential during sodiation, MoS_2 also suffers from sluggish kinetics of Na^+ ion diffusion and has an additional polysulfide shuttling issue.[14,15]

To overcome these obstacles, many researchers have been committed to improving the sodium storage ability of MoS_2 by designing novel architectures, preparing various composites, and controlling the size and morphology of electrode materials.[11,13,16–18] A general approach for enhancing the process is to design MoS_2 materials with different morphologies and shapes, for instance, 2D MoS_2 nanosheets, MoS_2 flowers, MoS_2 nanowalls, MoS_2 microspheres, MoS_2 nanotubes and MoS_2

[a]Department of Chemical Engineering, Hanyang University, Seoul 04763, Republic of Korea. E-mail: dongwonkim@hanyang.ac.kr; Fax: +82 2 2298 4101; Tel: +82 2 2220 2337

[b]Department of Chemical Engineering, Kyung Hee University, Yongin-si, Gyeonggi-do 17104, Republic of Korea

† Electronic supplementary information (ESI) available. See DOI: 10.1039/c9ta08839c

nanowires.[18–24] Another approach is the expansion of interlayer spacing to diminish the Na^+ ion diffusion barrier, including inserting some exotic atoms into the interlayers, physical or chemical exfoliation, and selective synthesis of MoS_2 with few layers with enlarged spacing, because it admits effective strain mitigation. Recently, Zhang *et al.* reported that an oxygen incorporation strategy to prepare enlarged interlayer spacing of MoS_2 nanosheets integrated with carbon fiber as an advanced anode material for SIBs.[25] An integration of 2D MoS_2 with carbonaceous materials such as amorphous carbon, graphene, and carbon nanotubes is a popular approach to accommodate the volume changes during a continuous charge–discharge process and enhance the structural stability.[26–29] For instance, Wang *et al.* reported vertically grown MoS_2 nanosheets over electrochemically exfoliated graphene nanosheets, and achieved excellent cycling and rate performance due to their high conductivity, satisfactory mechanical stability and abundant active sites.[18] Zhao *et al.* fabricated MoS_2 nanoflowers with wide interlayer spacing supported on carbon fibers (E-MoS_2/carbon fibers) and demonstrated their sodium storage ability for sodium-ion hybrid capacitors.[26] Jing *et al.* reported wide interlayer spacing, few-atomic-layered MoS_2 hollow spheres with N-doped monolayer carbon and studied their ion storage ability for LIBs and SIBs.[28] Liu *et al.* studied liquid exfoliated MoS_2 nanosheets percolated with single walled carbon nanotubes for high areal and volumetric SIBs.[29] Wang *et al.* reported MoS_2/amorphous carbon nanocomposites and studied their interfacial transitions between intercalation and conversion reactions for sodium storage ability.[30] However, all these approaches for enlarged interlayer spacing of MoS_2 are based on carbon-based templates, and to date there has been no study on the same 2D material as a core and shell with expanded interlayer spacing and it still remains a remarkable challenge.

Herein, for the first time, we synthesized vertically aligned interlayer expanded MoS_2 nanosheets integrated with carbon onto systematically optimized 2D MoS_2 nanorods and investigated their sodium storage performance. This approach involves an initial formation of two-dimensional MoS_2 nanorods (denoted as MoS_2 NRs) *via* systematically tuned surface sulfurized MoO_3 nanorods and subsequently wide spacing MoS_2 nanosheets concurrently with carbon were vertically aligned *via* a hydrothermal approach (named MoS_2@C@MoS_2). The electrocatalytic activity of MoS_2 and C is incorporated into an expanded 2D heterostructure over 2D MoS_2 NRs, which helps to accommodate the volume expansion during a continuous sodiation/de-sodiation process and eventually improve the reversibility of the electrode materials. An optimized MoS_2@C@MoS_2 anode delivered a high specific capacity and exhibited excellent cycling stability and rate performance.

Experimental details

Materials

Sodium molybdate dihydrate ($Na_2MoO_4 \cdot 2H_2O$), glucose ($C_6H_{12}O_6$), thiourea (N_2H_4CS), sulfur powder and carboxyl methyl cellulose were purchased from Sigma Aldrich. Concentrated nitric acid (conc. HNO_3), hydrogen peroxide (H_2O_2) and absolute ethanol were purchased from Daejung Chemicals Ltd. De-ionized (DI) water (resistivity: ~18.0 MΩ cm) was obtained from a Milli-Q water purification system and used throughout experiments.

Preparation of MoO_3 nanorods

MoO_3 nanorods were prepared using a hydrothermal method, as described elsewhere.[31] An appropriate amount of α-MoO_3 powder was mixed with 55 mL of aqueous H_2O_2 (30 wt%) and dissolved completely under stirring. Then 170 mL of distilled water and 27 mL of conc. HNO_3 were added to the above solution. Subsequently, the mixture was allowed to stand for 96 h at 25 °C. Then 60 mL of this mixture solution was shifted into an 80 mL capacity autoclave setup and heated to 170 °C for 24 h. After hydrothermal treatment, the autoclave was allowed to cool naturally, and then the greenish white precipitates were centrifuged with distilled water and absolute ethanol to clear away the impurity particles, and dried in air.

Preparation of MoS_2 nanorods

MoS_2 nanorods were prepared *via* a vapor phase ion-exchange method. A small amount of MoO_3 nanorods was weighed and kept inside a tubular furnace. A large amount of sulfur powder was carefully weighed and kept at the corner of the inlet side (as illustrated in Scheme 1). Then the furnace was heated to 500 °C at various ramp rates such as 5, 2, and 1 °C min^{-1} for 3 h under an argon/hydrogen (92 : 8 by volume) atmosphere. Pure MoS_2 nanorods could be obtained at a ramp rate of 1 °C min^{-1} and a standing time of 6 h. For comparison, MoO_2 nanorods were also prepared without a sulfur source at a ramp rate of 5 °C min^{-1} for 3 h.

Preparation of the MoS_2@C@MoS_2 core–shell structure

0.2 g of the as-prepared MoS_2 nanorods was dispersed in 100 mL of distilled water and kept under sonication and stirring. Then, a mixture of sodium molybdate dihydrate and thiourea (1 : 2 by weight) was added along with 0.25 g of glucose to the solution, and the solution was continuously stirred until all the precursors were completely dissolved. Eventually, a portion of the solution mixture was shifted to a stainless steel covered Teflon-lined autoclave and heated at 200 °C for 24 h. A black precipitate was then collected and dried in an electric oven at 80 °C overnight. Finally, the collected powder was annealed at 500 °C for 3 h under an argon atmosphere to obtain the MoS_2@C@MoS_2 powder.

Characterization

The crystal structure was characterized by X-ray diffraction (XRD) with Cu Kα radiation at a wavelength of 0.15045 nm using a D8 Bruker X-ray diffractometer at 2θ angles ranging from 5 to 80°. The morphology of the samples was investigated by using a SEM (NOVA Nano SEM-450) and HR-TEM (JEOL, JEM 2100F) equipped with an energy dispersive X-ray spectrometer (EDS). XPS spectra were recorded with a VG Multilab ESCA XPS (Model: 220i) with Mg/Al Kα radiation. N_2 adsorption and desorption

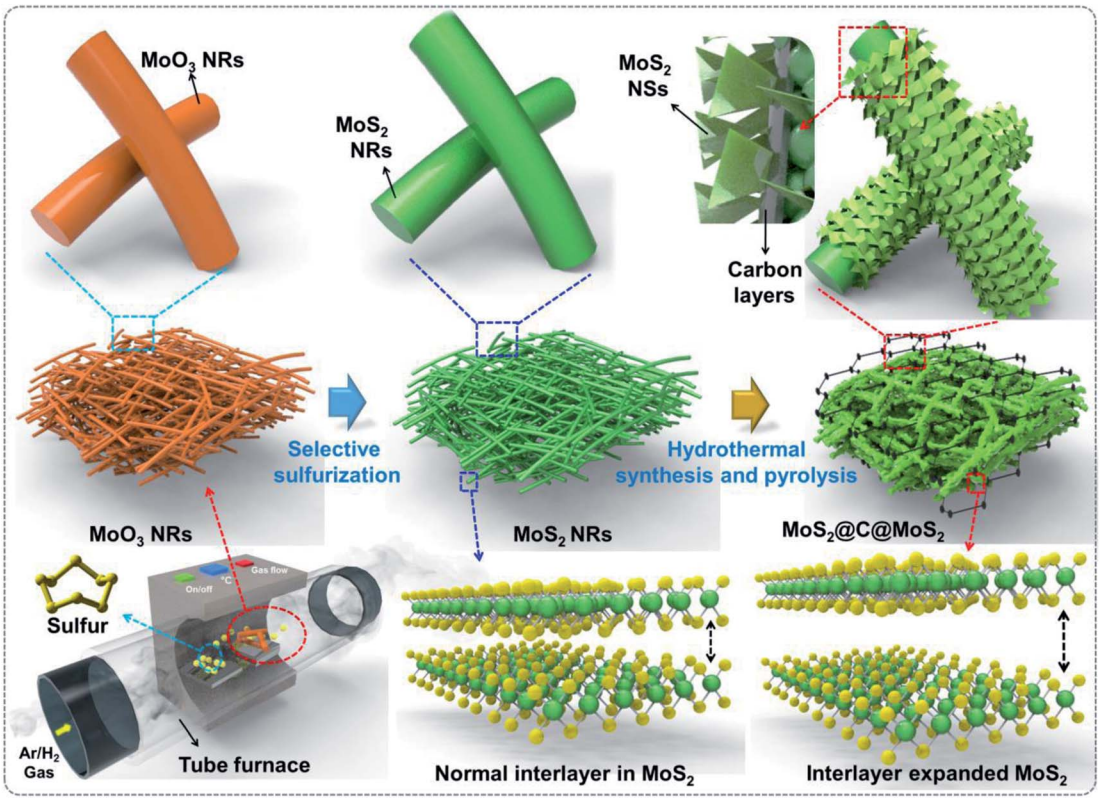

Scheme 1 Schematic illustration of the preparation of MoS_2@C@MoS_2 from MoO_3 nanorods *via* selective sulfurization and hydrothermal reactions.

isotherms were obtained using a specific surface area and pore distribution analyzer (ASAP-2020, micromeritics) at 77 K. Prior to the measurements, the sample was degassed at 300 °C for 2 h under vacuum. TGA was performed using a TGA/DTA/DSC analyzer (SDT Q600, Auto-DSCQ20 System). Cyclic voltammetry and electrochemical impedance spectroscopy were performed using a CHI600D electrochemical station. A charge and discharge cycling test was carried out using a WonA Tech equipment (WBCS 3000 model) at 25 °C.

Preparation of electrodes and cell assembly

The electrode was prepared by making a slurry *via* grinding of 70 wt% active material with 15 wt% Super-P carbon and 15 wt% carboxy methyl cellulose binder (15 wt%) using water. The homogeneous slurry was coated onto Cu foil and dried at 110 °C for 12 h under vacuum. The mass of the active material in the electrode was about 2.0 mg cm^{-2}. A CR2032-type coin cell was assembled by sandwiching a glass fiber separator (Whatman CAT no. 1823-047) between sodium foil (Alfa Aesar 99%) and the prepared electrode. An optimized liquid electrolyte comprising of 1.0 M $NaClO_4$ in ethylene carbonate (EC)/propylene carbonate (PC) (5 : 5 by volume, battery grade, PANAX ETEC Co. Ltd.) containing 10 wt% fluoroethylene carbonate (FEC) was used without further treatment.[32] A Mettler-Toledo coulometer was used to confirm that the content of water was less than 20 ppm in the liquid electrolyte. All the cells were assembled under an argon atmosphere inside a glove box. A sodium-ion full cell was fabricated with the MoS_2@C@MoS_2 anode and a $Na_3V_2(PO_4)_2F_3$ cathode. When assembling the sodium-ion full cell, the mass ratio of MoS_2@C@MoS_2 and $Na_3V_2(PO_4)_2F_3$ was optimized to 1.0 : 4.15 to obtain the best cycling performance. The cathode was prepared by mixing $Na_3V_2(PO_4)_2F_3$ (80 wt%), Super P carbon (10 wt%) and poly(vinylidene fluoride) (PVdF) binder (10 wt%) using *n*-methyl-2-pyrrolidone (NMP) solvent to make the slurry, and subsequently this slurry was pasted onto Al foil and dried in a vacuum oven at 110 °C for 12 h.

Results and discussion

The 2D-on-2D structured anode material was designed and synthesized by a two step approach, as schematically presented in Scheme 1. Briefly, hydrothermally prepared MoO_3 NRs were reduced with reduction gas at high temperature to form MoO_2 NRs. Subsequently, sulfur powder melts and sulfur vapor reacted with MoO_2 NRs to form MoS_2 NRs. Then, the fully formed MoS_2 NRs were subjected to hydrothermal treatment with sodium molybdate as the Mo source, thiourea as the S source and glucose as the carbon source. After hydrothermal treatment followed by carbonaceous reactions, an individual layer of MoS_2 along with carbon was uniformly aligned over the surface of the MoS_2 NRs. Fig. S1a† shows the XRD pattern of the hydrothermally prepared MoO_3 NRs. It revealed the formation of an orthorhombic phase of MoO_3 (JCPDS no. 35-0609) with well crystalline nature.[33] FE-SEM images show that the obtained

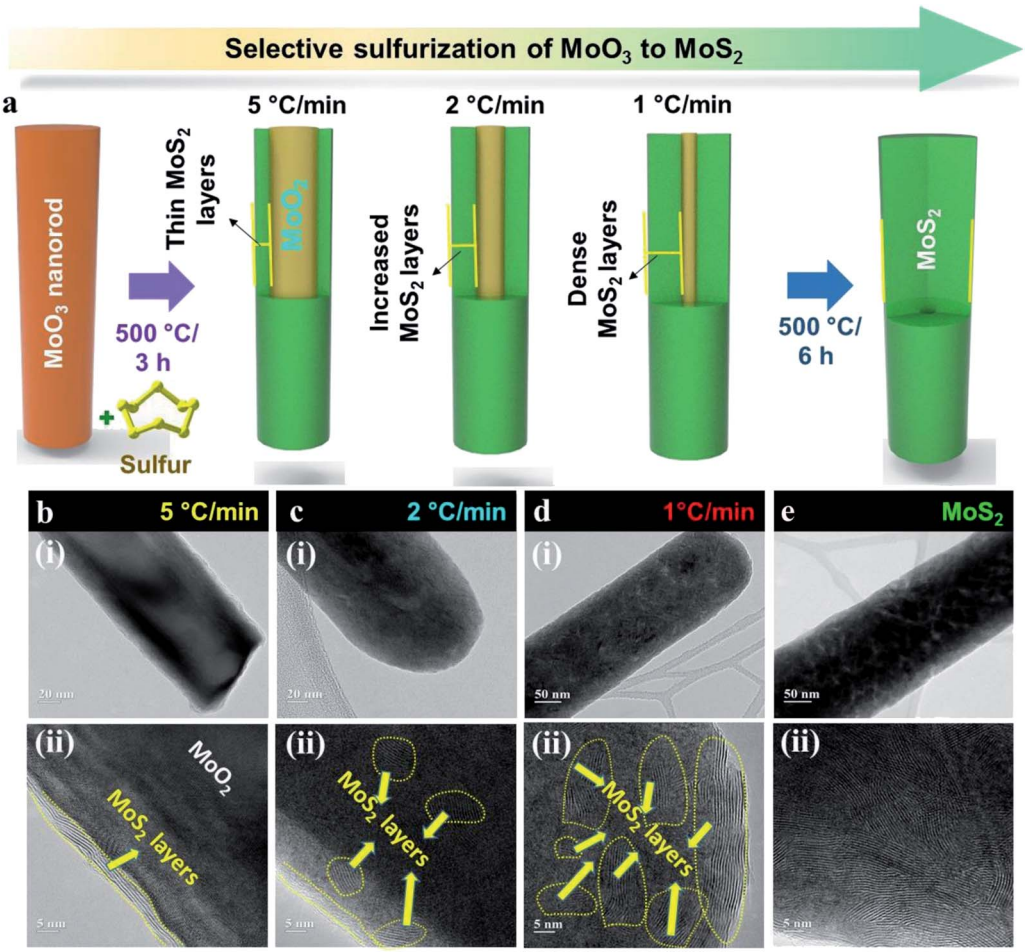

Fig. 1 (a) Schematic representation and corresponding (b–e) TEM (i) and HR-TEM (ii) images of the systematic formation of MoS_2 over the surface of MoO_3 nanorods *via* selective sulfurization by tuning the ramp rate.

MoO_3 had a uniform rod-like structure (Fig. S1b and c†). Fig. 1 demonstrates the selective sulfurization of MoO_3 NRs by stepwise ramp rate tuning. Firstly, the hydrothermally prepared MoO_3 NRs were subjected to a sulfurization reaction at the surface of the nanorods, whereas the sulfur source was kept in a separate crucible at the starting point of the heating mantle, as shown in Scheme 1. Upon the sulfurization reaction under different ramp rates such as 5, 2 and 1 °C min^{-1} at 500 °C with the sulfur source for 3 h, these MoO_3 NRs gradually turned into MoS_2-coated MoO_2 NRs and full MoS_2 was achieved at 1 °C min^{-1} for 6 h, as presented in the schematic illustration (Fig. 1a). TEM images of the corresponding transformation from MoO_3 into MoS_2 NRs are shown in Fig. 1b–e. At 5 °C min^{-1}, only the outer surface of the MoO_3 NRs was subjected to the sulfurization reaction due to the fast heating rate, whereas ramping rate of 2 and 1 °C min^{-1} provided a gradual improvement in the sulfurization reaction on the surface of molybdenum oxide. Finally, pure MoS_2 was successfully obtained at the heating rate of 1 °C min^{-1} for 6 h without any significant MoO_2 lattice fringes. The transformation mechanism of MoO_3 into MoS_2 NRs can be explained while understanding the molybdenum–oxygen–sulfur coordination chemistry as follows.[34,35] (i) The initial sulfurization reaction of MoO_3 NRs is accompanied by the reduction of Mo^{6+} to Mo^{5+} and subsequently the oxidation of sulfide ligands to bridge S_2^{2-}. (ii) Mo–O–Mo arrangements in MoO_3 vanish at low temperature, while additional terminal Mo=O_t (where t represents "transition") groups emerge, signifying that Mo–O–Mo structures were cleaved to form terminal Mo=O_t entities. (iii) The terminal Mo=O_t is the extreme reactive oxygen-containing species in oxysulfides, which disappears rapidly during heating, and subsequently the terminal Mo=O_t takes up sulfur atoms in the presence of reduction gas. (iv) The instability of Mo=O_t reacts either with H_2S gas (formed from the combination of H_2 and sulfur vapor at above 200 °C makes the protonation of O^{2-} ligands), subsequently by weakening of Mo=O and S–H bonds. Thereby, consuming of generated sulfur vapor by Mo moieties was occurred and eventually MoS_2 was formed at the high temperature reduction environment. Here, the partial sulfidation reaction occurred at the high ramp rate leaving the oxygen moiety, whereas the full oxygen moiety was consumed for the sulfurization reaction at the low ramp rate and full MoS_2 was formed at the long reaction time with a low ramp rate. The corresponding XRD patterns are presented in Fig. S2.† After

heating MoO_3 NRs at 500 °C, a reduction reaction occurred and pure MoO_2 NRs were formed in the absence of sulfur.[36] The crystalline peaks of MoO_2 NRs were well matched with the standard pattern (JCPDS card no. 32-0671), which belongs to the monoclinic phase. In the presence of sulfur at 5 °C min^{-1}, all the peaks were almost matched with those of pure MoO_2 with a slight rise of the MoS_2 peak at a 2θ of 14°. This peak gradually increased when decreasing the ramp rate to 2 and 1 °C min^{-1} along with new peaks at 33° for MoS_2, whereas the crystalline peaks of pure MoO_2 gradually decreased. At the end, pure MoS_2 was formed at the ramp rate of 1 °C min^{-1} for 6 h. All the crystalline peaks for pure MoS_2 are in good agreement with the standard pattern (JCPDS card no. 37-1492) for the hexagonal phase.[37] Fig. S3–S6† and 2a show the FE-SEM images of pristine MoO_2, the sulfurized sample at the ramp rates of 5, 2, and 1 °C min^{-1} and pristine MoS_2, respectively, at different magnifications. The rod-like morphology with a diameter in the range of 100–200 nm was well maintained even in high temperature reduction and sulfurization reactions. Fig. 2b(i–iii) present the TEM image (inset: SAED pattern), HR-TEM image and arrangement of atoms in pristine MoS_2 in which a rod-shaped morphology with a regular MoS_2 interval of 0.64 nm was achieved. Fig. 2c shows the FE-SEM images of the MoS_2@C@MoS_2 sample at different magnifications. It clearly reveals that the smooth MoS_2 NRs contain uniformly coarsened MoS_2 nanosheets (NSs) with carbon. The MoS_2@C NSs are about 50 nm thick surrounding the MoS_2 NRs, which was confirmed from the TEM image (Fig. 2d(i) and inset) with polycrystalline nature (confirmed from the SAED pattern). Interestingly, from the HR-TEM and FFT images (Fig. 2d(ii and

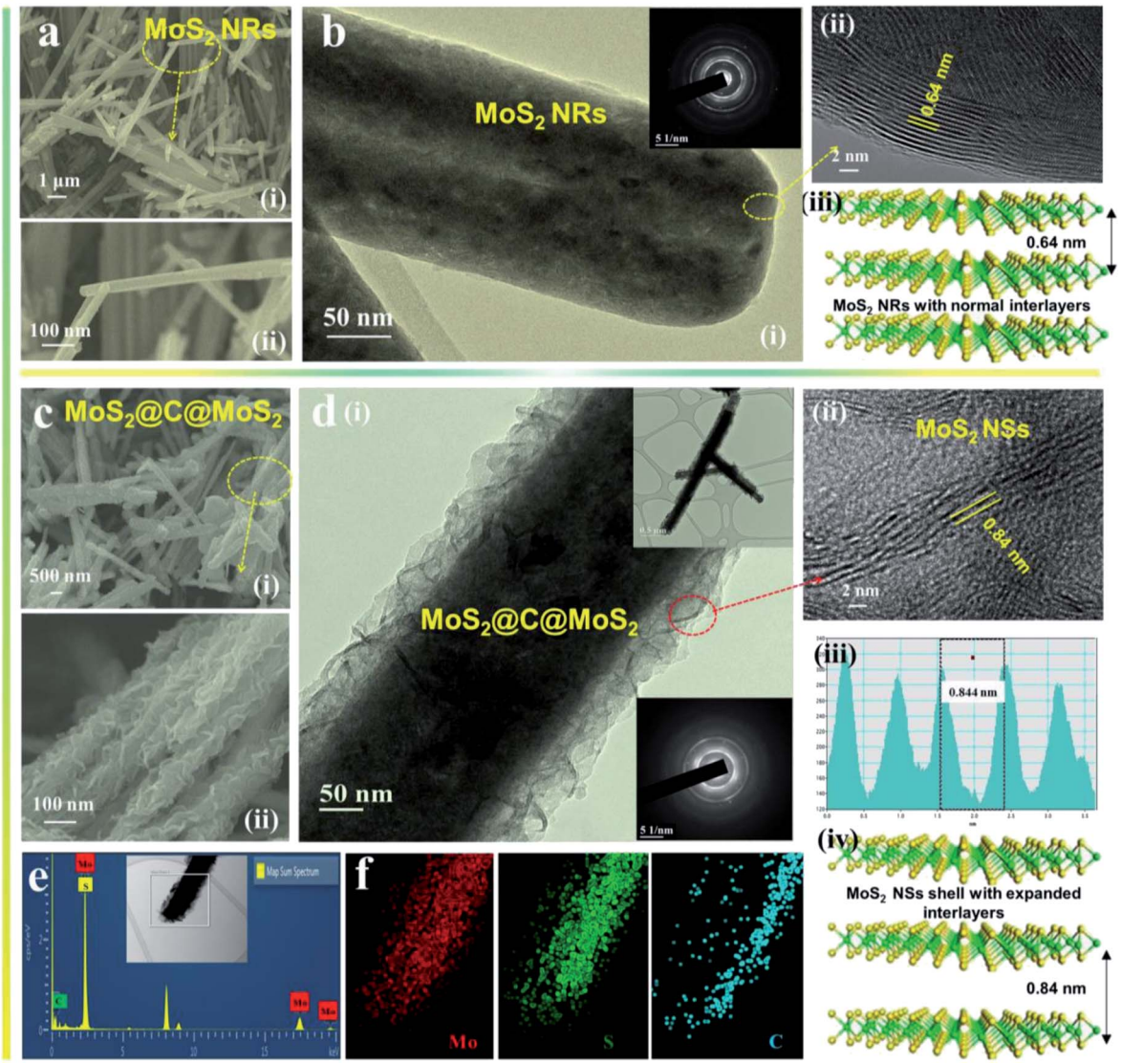

Fig. 2 (a) SEM images at (i) low and (ii) high magnification, (b) (i) TEM image (inset: SAED pattern), (ii) HR-TEM image, and (iii) crystal structure with normal interlayers of pristine MoS_2 NRs. (c) SEM images at (i) low and (ii) high magnification, (d) (i) TEM image (inset-top: low magnified; inset-bottom: SAED pattern), (ii) HR-TEM image, (iii) FFT image, (iv) crystal structure with expanded interlayers of MoS_2 NSs, (e) EDS spectrum, (inset – scanned part) and (f) EDS mapping with the elements of Mo, S and C of the MoS_2@C@MoS_2 sample.

iii)) the expanded interlayer spacing of MoS_2 NSs over MoS_2 NRs was observed to be 0.84 nm. The carbon layer was formed from glucose during annealing and this layer was sandwiched between two adjacent MoS_2 monolayers, which facilitates the expanded interlayer spacing. This enlarged interlayer spacing of MoS_2 NSs with carbon layers resides especially on the outer surface, which provides an easy conduction pathway for electrolyte ions to utilize the inner MoS_2 NRs. Fig. 2d(iv) presents the crystal structure of MoS_2 with enlarged interlayer spacing. Fig. S7† shows the EDS spectra of various sulfurized samples. As clearly seen in the results, the atomic content of oxygen gradually decreased with decreasing the ramp rate. In the full MoS_2 sample, the atomic percentage of oxygen was almost negligible (only 0.82%) as compared to other sulfurized samples (5, 2, and 1 °C min^{-1} sulfurized samples). Such an abrupt decrease in the oxygen content indicates that almost all the molybdenum oxides were converted to MoS_2 except for a very small amount of MoO_2. Fig. 2e and f depict the EDS spectrum and corresponding EDS mapping images of MoS_2@C@MoS_2, which clearly confirm the exact atomic ratio and uniform distribution of Mo, S and C in the prepared materials.

XRD patterns of pristine MoS_2 and MoS_2@C@MoS_2 are shown in Fig. 3a. The broad diffraction peaks at 13.8, 33.2, 39.3 and 58.7° for the MoS_2@C@MoS_2 sample correspond to the (002), (101), (103) and (110) planes of hexagonal MoS_2, respectively, which are in good agreement with those of the pristine MoS_2 NRs. In addition, a small broad peak was observed at 9.0°, which indicates the presence of expanded interlayer spacing of MoS_2 NSs.[38,39] Furthermore, the presence of carbon was confirmed from the peak at 26.0°, corresponding to the (002) plane of C. In the pristine MoS_2 sample, a very small peak was observed at around 26.0°, which might be due to the presence of a very small amount of MoO_2. This result is consistent with the EDS results (Fig. S7†) showing that there is a negligible amount of oxygen (0.82 atomic%) in the full MoS_2 sample, as previously discussed. Brunauer–Emmett–Teller (BET) measurement was performed to calculate the specific surface area of the pristine MoS_2 NR and MoS_2@C@MoS_2 samples (Fig. 3b). Due to the rough porous structure and ultrathin NSs, the MoS_2@C@MoS_2 sample has a large surface area of 28.1 m^2 g^{-1}, which is about three times larger than that of the pristine MoS_2 NRs (9.0 m^2 g^{-1}). Such a high surface area and porous structure will be advantageous for the fast transport of ions and mitigating the volume expansion of MoS_2 during continuous charge and discharge cycles. In order to measure the content of carbon and MoS_2 in the MoS_2@C@MoS_2 sample, TGA analysis was conducted (Fig. 3c). According to TGA analysis, the MoS_2 content in MoS_2@C@MoS_2 was calculated to be 85.8 wt%. To investigate the interaction between MoS_2 and C in MoS_2@C@MoS_2, XPS analysis was performed for pristine MoS_2 and MoS_2@C@MoS_2 samples. Mo3d, S2p and C1s core-level spectra of pristine MoS_2 and MoS_2@C@MoS_2 are shown in Fig. 3d–f. A pair of peaks centered at 232.2 and 229.0 eV have been noticed for the Mo3d core-level spectrum in MoS_2 NRs (Fig. 3d), which can be assigned to $Mo3d_{3/2}$ and $Mo3d_{5/2}$, respectively. In addition, one more small peak was observed at a binding energy of 226.0 eV, which was matched with the S2s spectrum.[40] Meanwhile, a pair of peaks centered at 162.9 and 161.7 eV were observed for the S2p core-level spectrum of MoS_2 NRs, which can be attributed to $S2p_{1/2}$ and $S2p_{3/2}$, respectively. This result suggests the presence of Mo^{4+} and S^{2-} in the pristine MoS_2 NRs. Fig. 3f shows the presence of sp^2C and sp^3C at 284.4 and 285.3 eV, respectively. As

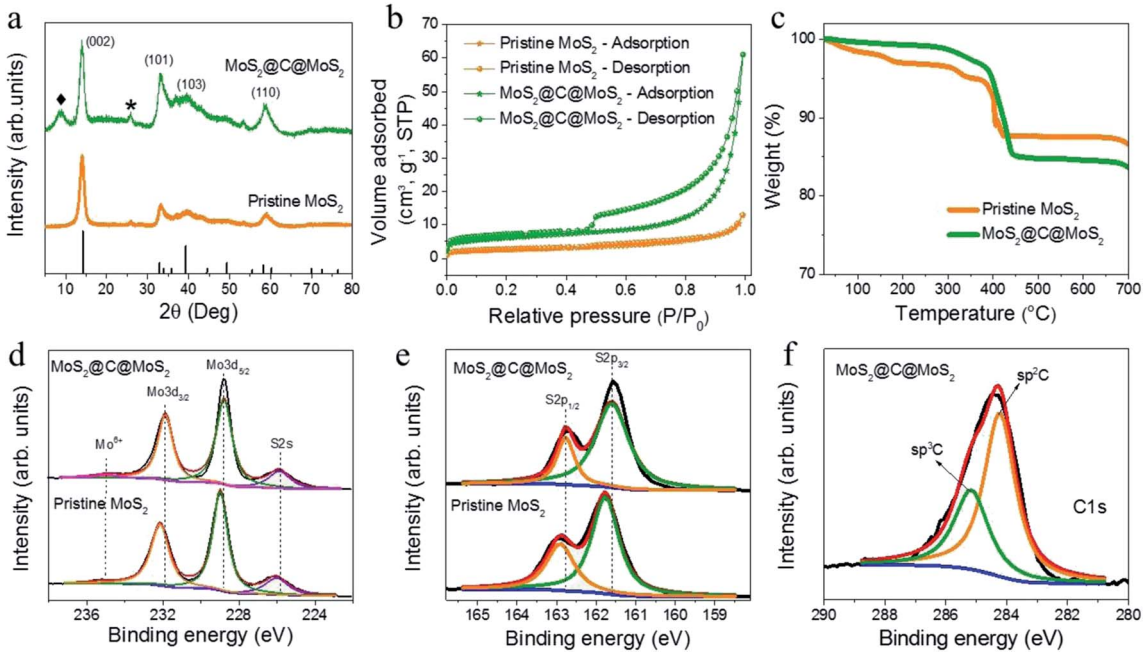

Fig. 3 (a) XRD patterns [◆: (001) plane of MoS_2], (b) N_2 adsorption and desorption isotherm, and (c) TGA curves and XPS spectra; (d) Mo3d core-level and (e) S2p core-level of pristine MoS_2 and MoS_2@C@MoS_2 and (f) C1s core level spectrum of MoS_2@C@MoS_2.

presented in Fig. 3d and e, Mo3d and S2p core-level spectra for the MoS_2@C@MoS_2 sample downshifted towards lower binding energy, indicating increased electron cloud density in the vicinity of MoS_2.[41,42] Concurrently, the characteristic peak of C1s core-level spectra for the MoS_2@C@MoS_2 sample upshifted towards higher binding energy compared the characteristic peak of C1s in pure carbon, which manifests the electron clouds around MoS_2 shared by the increased oxidation state of C.[41] This indicates that the bias from carbon and MoS_2 appeared from the improved synergy between the larger electronegativity and distinct valence-band potentials of molybdenum and carbon, thereby originating a robust connection and evolution of a heterojunction between MoS_2 NSs and carbon layers.[43]

Stimulated by the above hierarchical structure and heterojunction design, the sodium storage ability of the MoS_2@C@MoS_2 material was comprehensively investigated in a coin-cell-type configuration *via* electrochemical impedance spectroscopy (EIS), charge–discharge cycles and cyclic voltammetry (CV). Fig. 4a displays the Nyquist plot at the open circuit potential in the frequency range of 0.01 to 1 M Hz for pristine MoS_2 and MoS_2@C@MoS_2 electrodes, respectively. Both spectra consist of a concaved semicircle region in the high and medium frequency regions and a slanted straight line in the lower frequency region, which indicate charge transfer resistance (R_{ct}) at the electrode/electrolyte interface and Na^+ ion diffusion within the electrode, respectively. As can be seen in Fig. 4a, the charge transfer resistance was much lower for the MoS_2@C@MoS_2 electrode than that of the pristine MoS_2 electrode. The slanted line signifying the ion diffusion is steeper for the MoS_2@C@MoS_2 electrode, indicating the facilitated Na^+ ion diffusion, which originates form the existence of an enlarged interlayer spacing of MoS_2 NSs with a highly conducting carbon network. To evaluate the specific capacity of the prepared electrodes, galvanostatic charge and discharge cycling was performed in the voltage range of 0.01 to 3.0 V for 100 cycles at a constant current density of 100 mA g^{-1} after two formation cycles at 50 mA g^{-1}. The MoO_3 NR electrode initially delivered a discharge capacity of 160.0 mA h g^{-1} with an initial coulombic

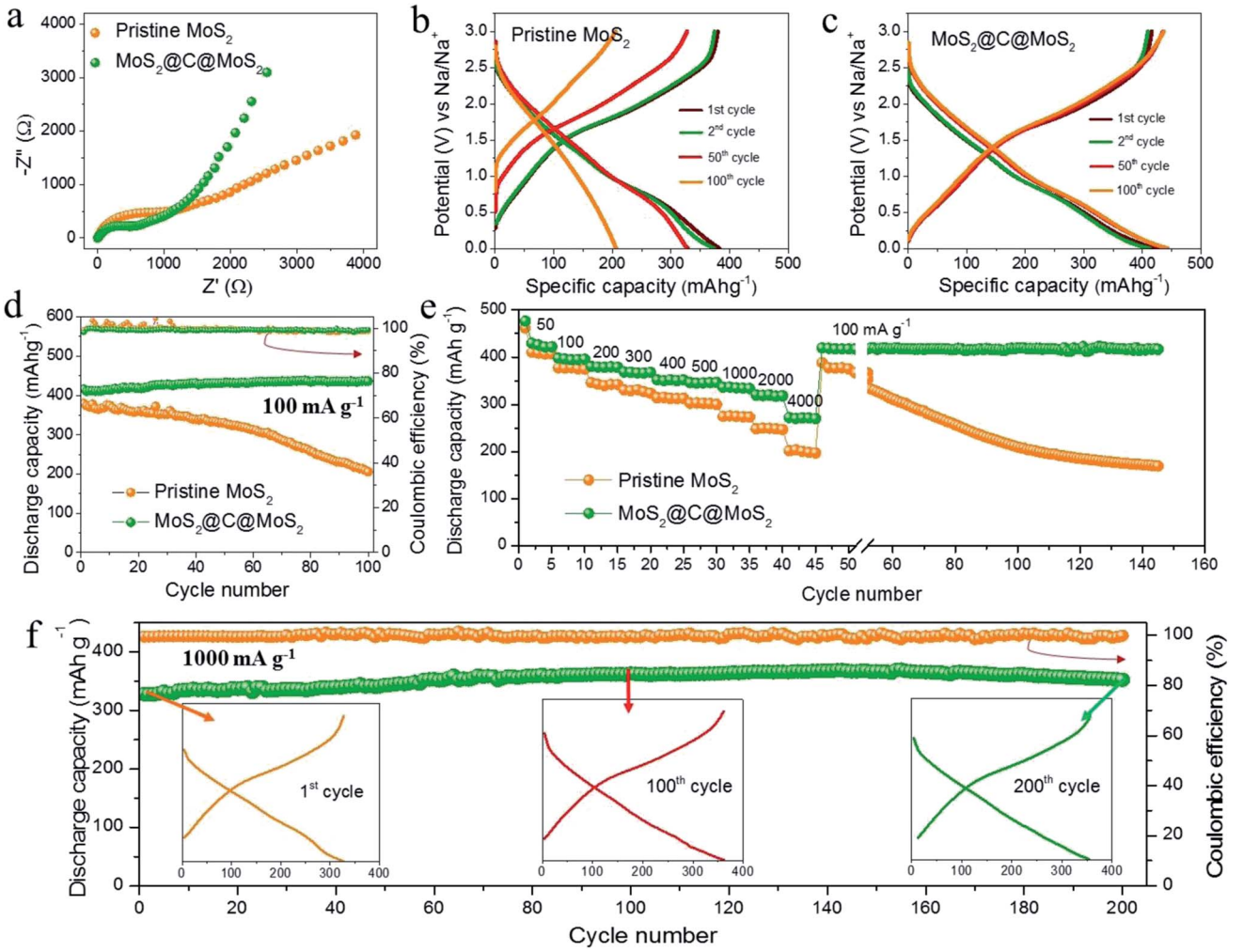

Fig. 4 (a) Nyquist plot, (b and c) charge and discharge curves, (d) cycling stability at 100 mA g^{-1} after two formation cycles, (e) rate capability at various current densities for pristine MoS_2 and MoS_2@C@MoS_2 electrodes and (f) cycling performance of the MoS_2@C@MoS_2 electrode at 1 A g^{-1} (inset: charge and discharge curves in the 1st, 100th and 200th cycles, respectively).

efficiency (ICE) of 45.7% (Fig. S8a†). After 100 cycles, the discharge capacity decreased to 124.8 mA h g^{-1}, which corresponded to 78.0% of its initial discharge capacity. Rate capability at current densities from 50 to 4000 mA g^{-1} in Fig. S8b† reveals poor performance for MoO_3 NRs. After sulfidation reaction at 5 °C min^{-1}, the discharge capacity significantly increased to 259 mA h g^{-1} at 100 mA g^{-1} with an ICE of 79.0% at 50 mA g^{-1} (Fig. S9a†). The discharge capacity was well maintained up to 75 cycles, and then gradually started to decrease to 247 mA h g^{-1} in the 100th cycle. Even though the 5 °C min^{-1} electrode exhibited relatively good rate performance, its capacity drastically decreased at high current density and dropped to a lower value after 75 cycles at 100 mA g^{-1} (Fig. S9b†). In the case of 2 and 1 °C min^{-1} electrodes (Fig. S10a and S11a†), the discharge capacity gradually increased up to 360 and 392 mA h g^{-1}, respectively, and drastic capacity fading was observed after that. Similarly, poor rate performance was observed with a drastic drop in discharge capacity for the subsequent low current cycling (Fig. S10b and S11b†). The enhanced specific capacity at a lower ramp rate can be attributed to the increment in the sulfur content in MoS_2 NRs, and the capacity was maintained until the sodium ion diffusion occurred in the MoS_2 region. The drastic drop in capacity might be due to the presence of MoO_2 in the inner core of the MoS_2 NRs, which originates from the conversion reaction of sodium ions with MoO_2 NRs (see Fig. S12 in the ESI† for pristine MoO_2 NRs). Fig. 4b and c show the typical charge and discharge curves for pristine MoS_2 and MoS_2@C@MoS_2 electrodes at a current density of 100 mA g^{-1} after two formation cycles at 50 mA g^{-1}. A high initial discharge capacity of 477 mA h g^{-1} was achieved with an improved ICE of 86.3% for the MoS_2@C@MoS_2 electrode, whereas 460 mA h g^{-1} was achieved for the pristine MoS_2 electrode. After formation cycles, a discharge capacity of 417 mA h g^{-1} was attained at 100 mA g^{-1} for the MoS_2@C@MoS_2 electrode, whereas only 379 mA h g^{-1} was obtained for the pristine MoS_2 electrode. Capacity fading was observed for the pristine MoS_2 electrode, whereas almost a constant capacity was maintained for the MoS_2@C@MoS_2 electrode, revealing its excellent cycling stability (Fig. 4d). Subsequently, rate performance was investigated for pristine MoS_2 and MoS_2@C@MoS_2 electrodes, and the results are presented in Fig. 4e. As expected, higher specific capacity was achieved for the MoS_2@C@MoS_2 electrode as compared to that of the pristine MoS_2 electrode. More importantly, the MoS_2@C@MoS_2 electrode delivered a high discharge capacity of 352 mA h g^{-1} after 200 cycles at 1000 mA g^{-1} (Fig. 4f). Charge and discharge curves in the 1st, 100th and 200th cycles (inset of Fig. 4f) demonstrate that the voltage profiles do not change significantly in the subsequent cycles. Compared with most other transition metal sulfide compounds and MoS_2-based electrodes for SIBs, the MoS_2@C@MoS_2 electrode prepared in this study exhibited better electrochemical performance in terms of cycling stability and rate capability (see Tables S1 and S2 in the ESI†).

Furthermore, the electrochemical kinetics of the MoS_2@C@MoS_2 electrode was evaluated by cyclic voltammetry, and the results are presented in Fig. 5. As shown in Fig. 5a, during the first cathodic scan, the peak observed at 0.7 V was ascribed to the conversion of sodium ions into MoS_2 interlayers (Na_xMoS_2)

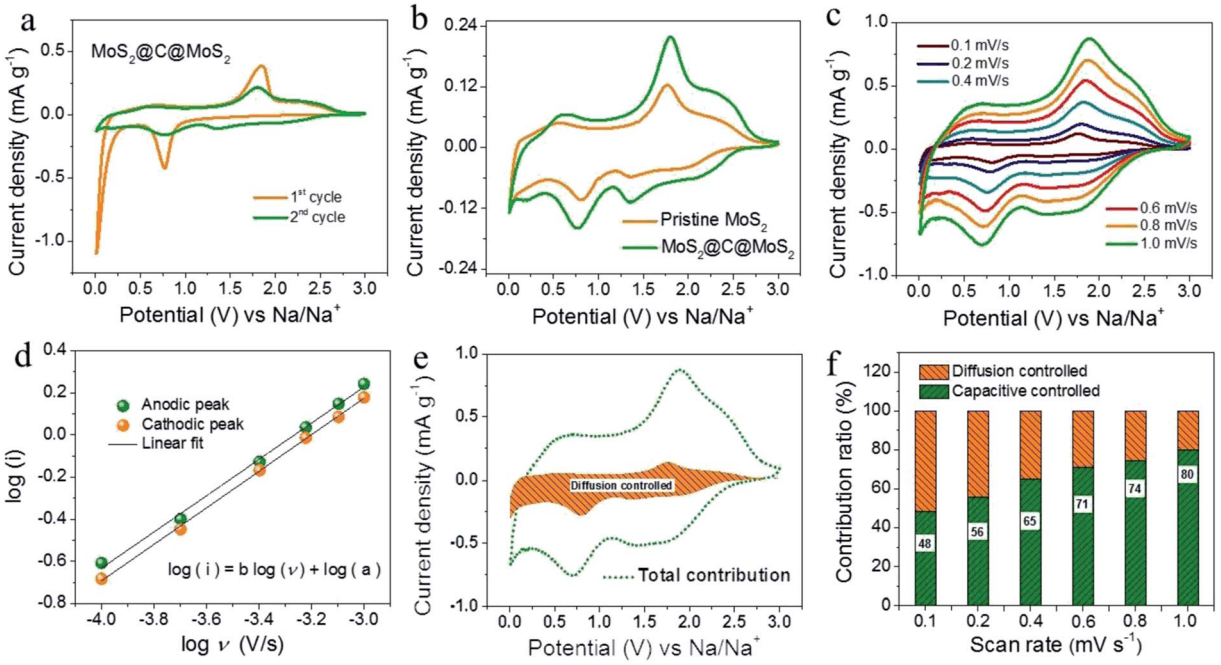

Fig. 5 Cyclic voltammograms of (a) the MoS_2@C@MoS_2 electrode for the first 2 cycles at 0.1 mV s^{-1}, (b) comparison of cyclic voltammograms of pristine MoS_2 and MoS_2@C@MoS_2 electrodes at 0.1 mV s^{-1}, (c) cyclic voltammograms of the MoS_2@C@MoS_2 electrode at various scan rates from 0.1 to 1.0 mV s^{-1}, (d) linear fit curve for logarithmic plot of peak current *vs.* scan rate for the MoS_2@C@MoS_2 electrode, and (e) cyclic voltammograms for differentiating the diffusion controlled process from the total contribution, (f) relative contribution of diffusion and capacitive controlled reactions at various scan rates for the MoS_2@C@MoS_2 electrode.

and the formation of a solid electrolyte interphase (SEI) layer.[44,45] Then, the sharp peak below 0.3 V was attributed to the conversion of Na_xMoS_2 to Mo and Na_2S.[46,47] During the first anodic scan, the peak at 1.78 V can be ascribed to the oxidation of Mo to MoS_2.[48] In the second cycle, a peak at 1.2 V was clearly visible, which can be assigned to the intercalation of sodium ions into MoS_2 interlayers. The intensity of the peak at 0.7 V during the cathodic scan decreased from the second cycle due to the formation of a stable SEI film. Both reduction and oxidation peaks were overlaid in the successive cycles, suggesting its excellent reversibility. These peaks are almost matched with those of pristine MoS_2, as presented in Fig. 5b, with a larger integral area under the CV curve, indicating the improved sodium storage capacity of the MoS_2@C@MoS_2 electrode. Fig. 5c and d present the CV curves of the MoS_2@C@MoS_2 electrode at various scan rates and the corresponding logarithmic plot of current (i) *vs.* scan rate (v) for the anodic and cathodic peaks, respectively. According to the power law $i = a \times v^b$,[49] the charge storage mechanism can be investigated by using the linear fit of log v *vs.* log i. Specifically, a b value of 0.5 signifies the linear dominance of a diffusion governed reaction, whereas a b value of 1.0 implies the dominance of a surface governed reaction in a capacitive process. By plotting the linear fit of log v *vs.* log i as shown in Fig. 5d, the b value was determined to be 0.87 and 0.86 for anodic and cathodic peaks, respectively, indicating the dominance of the surface governed capacitive process (whereas the b value was determined to be 0.83 and 0.81 for the pristine MoS_2 electrode for respective peaks). The diffusion coefficient of Na^+ ions was calculated using the Randles–Sevcik equation based on cyclic voltammetry results.[50,51] The calculated diffusion coefficient of Na^+ ions in the MoS_2@C@MoS_2 electrode is 1.2×10^{-8} cm^2 s^{-1}, which is much higher than that measured for the pristine MoS_2 electrode (1.3×10^{-9} cm^2 s^{-1}). These results clearly indicate that the diffusion of Na^+ ions is more facile in the MoS_2@C@MoS_2 electrode, which results in enhanced rate capability. To evaluate the descriptive charge storage mechanism, the equation $i = k_1v + k_2v^{1/2}$ was further applied. In this equation, k_1v represents the capacitive dominance and $k_2v^{1/2}$ stands for the diffusion dominance, where constants k_1 and k_2 can be calculated by

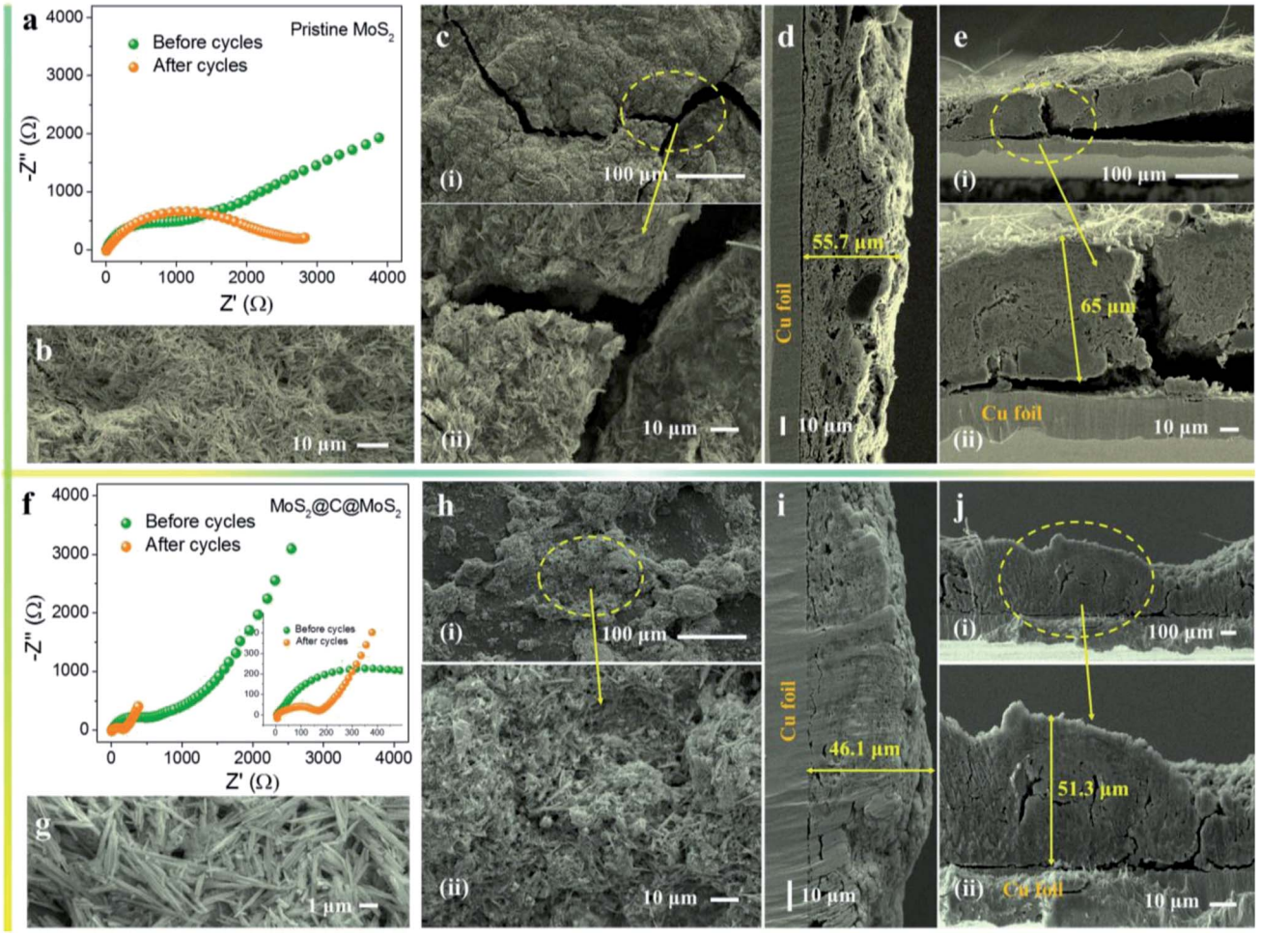

Fig. 6 (a) Nyquist plot before and after cycles, surface FE-SEM images (b) before and (c) after cycles at different magnifications, and cross-sectional FE-SEM images (d) before and (e) after cycles at different magnifications for the pristine MoS_2 electrode. (f) Nyquist plot before and after cycles, surface FE-SEM images (g) before and (h) after cycles at different magnifications, and cross-sectional FE-SEM images (i) before and (j) after cycles at different magnifications for the MoS_2@C@MoS_2 electrode (*ex situ* FE-SEM has been performed after 100 cycles at 100 mA g^{-1}).

plotting $\nu^{1/2}$ *vs.* $i \times \nu^{-1/2}$ (Fig. S13†).[52] Fig. 5f presents the relative contribution of diffusion and capacitive controlled reactions in the MoS_2@C@MoS_2 electrode at different scan rates. The capacitive contribution increased from 48 to 80% when the scan rate increased from 0.1 to 1.0 mV s^{-1}, whereas only 71% was achieved in pristine MoS_2 at 1.0 mV s^{-1} (Fig. S14†). These results suggest that the capacitive contribution dominates the total capacity of the MoS_2@C@MoS_2 electrode. The improved charge transfer kinetics and fast surface capacitive storage of the MoS_2@C@MoS_2 electrode can be attributed to the effective exposure of vertically aligned MoS_2 NSs, the interior pathways between interconnected NSs and the close contact of MoS_2 with conducive carbon.

In order to understand the cycling performance of pristine MoS_2 and MoS_2@C@MoS_2 electrodes, EIS and *ex situ* FE-SEM analyses are employed, and the results are presented in Fig. 6. After 100 cycles, the value of R_{ct} drastically increased for the pristine MoS_2 electrode (as shown in Fig. 6a), which was due to the increment in the internal resistance of active materials by detachment of electrode materials from the Cu substrate. This could be confirmed from the FE-SEM images before (Fig. 6b) and after (Fig. 6c) cycles. As shown in Fig. 6b, an even surface was observed in the electrode before cycles and this smooth surface was almost ruptured with large number of cracks after continuous cycles (Fig. 6c). Also, the interfacial contact between the current collector and MoS_2 electrode was examined *via* cross-sectional FE-SEM images. Good adhesion of the electrode to the Cu foil was seen in the fresh MoS_2 electrode with an average thickness of 55.7 μm. After charge and discharge cycles, the contact of the pristine MoS_2 electrode with the Cu substrate was almost fully ruptured, besides the average thickness of the electrode increased to 65.0 μm. It might be due to the incapability of pristine MoS_2 for accommodating the guest material. Such a drawback of the pristine MoS_2 electrode was alleviated by the MoS_2@C@MoS_2 heterostructure. As can be seen in Fig. 6f, R_{ct} significantly decreased after 100 cycles with better Warburg diffusion. After cycles, the surface morphology of the MoS_2@C@MoS_2 electrode (Fig. 6h) was almost identical to that of the fresh electrode (Fig. 6g) except for typical aggregation of the electrode during continuous charge and discharge cycles. In view of cross-section images for the MoS_2@C@MoS_2 electrode, a good adhesion to the Cu substrate was observed with no remarkable changes in the thickness of the electrode even after continuous sodiation and desodiation cycles.[53] These results demonstrate that the heterostructured MoS_2@C@MoS_2 electrode has the capability of controlling the volume expansion during continuous cycling by facilitating strong bonding of interconnected MoS_2 NSs and conducive carbon to the Cu current collector.

The MoS_2@C@MoS_2 electrode can be used as a promising anode material for SIBs, because it has higher specific capacity than that of hard carbon. Herein, a full SIB was fabricated using MoS_2@C@MoS_2 as an anode and $Na_3V_2(PO_4)_2F_3$ (NVPF) as a cathode material. XRD and FE-SEM images of NVPF are shown in Fig. S15a and b,† respectively, which indicate highly crystalline nature without any other impurities (assigned to JCPDS PDF: 0.1-0.12-2207) and the plate-like morphology of NVPF. The NVPF electrode exhibited good cycling stability (with CE > 99%) at 100 mA g^{-1} and rate capability (Fig. S15c and d†). A schematic representation of an assembled sodium-ion full cell is shown in Fig. 7a. Fig. 7b presents the CV curves of the anode and cathode at a scan rate of 1.0 mV s^{-1}. Particularly, cyclic voltammetry of

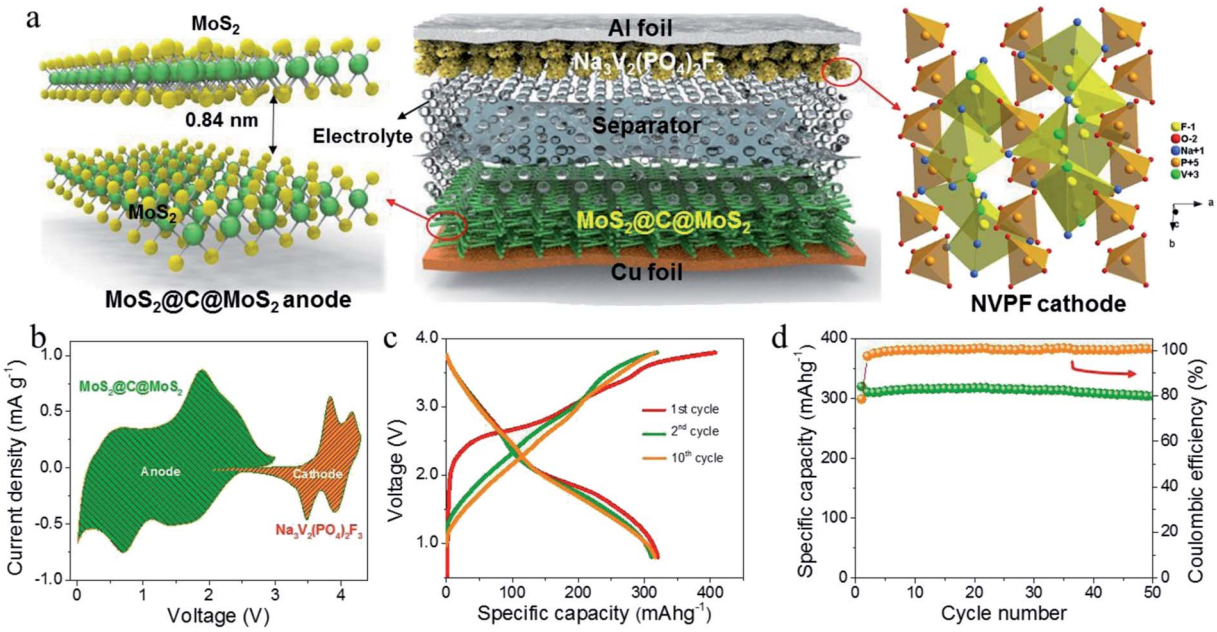

Fig. 7 (a) Schematic illustration of the sodium-ion full cell comprising of the MoS_2@C@MoS_2 anode and a $Na_3V_2(PO_4)_2F_3$ (NVPF) cathode, (b) CV curves of the anode and cathode at a scan rate of 1.0 mV s^{-1}, (c) charge and discharge curves of the assembled full cell in the voltage range of 0.8–3.8 V and (d) cycling performance of the assembled MoS_2@C@MoS_2||NVPF full cell at 50 mA g^{-1} (note that the specific capacity was calculated based on the mass of the anode material).

NVPF was performed in the potential range of 2.0–4.3 V *versus* Na/Na^+, in which a pair of reversible redox peaks were shown, attributed to the insertion and extraction of sodium ions. During the anodic scan, two peaks at 3.8 and 4.15 V are due to the extraction of Na from the NASICON structure, and conversely during the cathodic scan, the two peaks at 3.5 and 3.9 V are associated with the insertion of Na. Fig. 7c shows the charge and discharge curves of the assembled full cell in the voltage range of 0.8–3.8 V. The first cycle delivered a discharge capacity of 320 mA h g^{-1} with an ICE of 78.5%. The subsequent cycles were well overlapped with the second cycle with a high CE of >99.5%. At the end of 50 continuous cycles, a discharge capacity of 305 mA h g^{-1} was maintained with a CE of ~100%, which is comparable to that of recent sulfide-based full cells. Based on the above results, the designed MoS_2@C@MoS_2 heterostructure would be an auspicious anode material for SIBs.

Conclusions

We synthesized vertically grown MoS_2@C nanosheets with wide interlayer spacing over MoS_2 nanorods by modulating the vapor phase and growth process for high performance SIB anodes. By regulating the contiguous geometry of the electrode material, enhanced cycling stability and rate performance could be achieved in this work. Such a superior performance is predominantly due to fact that the interconnection of MoS_2 and carbon NSs suppresses the additional formation of SEI layers and mitigates the structural degradation of inner MoS_2 NRs. Furthermore, the heterostructured design improved the specific surface area, electronic conductivity and capacitive contribution. As a result, the MoS_2@C@MoS_2 electrode exhibited a discharge capacity of 417 mA h g^{-1} at 100 mA g^{-1} with good capacity retention and excellent rate capability. A sodium-ion full cell comprised of the MoS_2@C@MoS_2 anode and a $Na_3V_2(PO_4)_2F_3$ cathode maintained a specific capacity of 305 mA h g^{-1} after 50 continuous cycles, demonstrating that the MoS_2@C@MoS_2 material can be considered as an encouraging anode for SIBs.

Conflicts of interest

The authors declare no conflict of interest.

Acknowledgements

This work was supported by the National Research Foundation of Korea (NRF) funded by the Korean Government (2017R1C1B2012700 and 2017R1A2A2A05020947) and the BK21 plus program through the NRF funded by the Ministry of Education of Korea.

References

1 D. Larcher and J.-M. Tarascon, *Nat. Chem.*, 2015, **7**, 19.
2 N. Nitta, F. Wu, J.-T. Lee and G. Yushin, *Mater. Today*, 2015, **18**, 252.
3 J.-W. Choi and D. Aurbach, *Nat. Rev. Mater.*, 2016, **1**, 16013.
4 H.-S. Kim, H.-G. Kim, Z. Ding, M.-H. Lee, K.-M. Lim, G. Yoon and K.-S. Kang, *Adv. Energy Mater.*, 2016, **6**, 1600943.
5 Y. Naoaki, K. Kei, D. Mouad and K. Shinichi, *Chem. Rev.*, 2014, **114**, 11636.
6 D. Sun, D. Ye, P. Liu, Y. Tang, J. Guo, L. Wang and H. Wang, *Adv. Energy Mater.*, 2018, **8**, 1702383.
7 Y. Subramanian, G. K. Veerasubramani, M.-S. Park and D.-W. Kim, *J. Electrochem. Soc.*, 2019, **166**, A598.
8 T. Zhou, W.-K. Pang, C. Zhang, J. Yang, Z. Chen, H.-K. Liu and Z. Guo, *ACS Nano*, 2014, **8**, 8323.
9 W. Li, J. Huang, L. Feng, L. Cao, Y. Feng, H. Wang, J. Li and C. Yao, *J. Mater. Chem. A*, 2017, **5**, 20217.
10 D. Su, S. Dou and G. Wang, *Chem. Commun.*, 2014, **50**, 4192.
11 T. Wang, S. Chen, H. Pang, H. Xue and Y. Yu, *Adv. Sci.*, 2017, **4**, 1600289.
12 T. Stephenson, Z. Li, B. Olsen and D. Mitlin, *Energy Environ. Sci.*, 2014, **7**, 209.
13 Y.-X. Wang, S.-L. Chou, D. Wexler, H.-K. Liu and S.-X. Dou, *Chem.–Eur. J.*, 2014, **20**, 9607.
14 D. Sun, D. Ye, P. Liu, Y. Tang, J. Guo, L. Wang and H. Wang, *Adv. Energy Mater.*, 2018, **8**, 1702383.
15 X. Xu, R. Zhao, W. Ai, B. Chen, H. Du, L. Wu, H. Zhang, H. Huang and W. Yu, *Adv. Mater.*, 2018, **30**, 1800658.
16 Y. Li, R. Zhang, W. Zhou, X. Wu, H. Zhang and J. Zhang, *ACS Nano*, 2019, **15**, 5533.
17 Y. Zhang, H. Tao, S. Du and X. Yang, *ACS Appl. Mater. Interfaces*, 2019, **11**, 11327.
18 G. Wang, J. Zhang, S. Yang, F. Wang, X. Zhuang, K. Müllen and X. Feng, *Adv. Energy Mater.*, 2018, **8**, 1702254.
19 Z. Hu, L.-X. Wang, K. Zhang, J.-B. Wang, F.-Y. Cheng, Z.-L. Tao and J. Chen, *Angew. Chem.*, 2014, **126**, 13008.
20 Z.-T. Shi, W.-P. Kang, J. Xu, Y.-W. Sun, M. Jiang, T.-W. Ng, H.-T. Xue, D.-W. Yu, W. Zhang and C.-S. Lee, *Nano Energy*, 2016, **22**, 27.
21 D.-W. Su, S.-X. Dou and G.-X. Wang, *Adv. Energy Mater.*, 2015, **5**, 1401205.
22 S.-H. Choi, Y.-N. Ko, J.-K. Lee and Y.-C. Kang, *Adv. Funct. Mater.*, 2015, **25**, 1780.
23 X. Zhang, X. Li, J. Liang, Y. Zhu and Y. Qian, *Small*, 2016, **18**, 2484.
24 S. Liu, Y. Yin, M. Wu, K.-S. Hui, K.-N. Hui, C.-Y. Ouyang and S.-C. Jun, *Small*, 2019, **15**, 1803984.
25 Y. Zhang, H. Tao, T. Li, S. Du, J. Li, Y. Zhang and X. Yang, *ACS Appl. Mater. Interfaces*, 2018, **10**, 35206.
26 C. Zhao, C. Yu, M. Zhang, Q. Sun, S. Li, M.-N. Banis, X. Han, Q. Dong, J. Yang, G. Wang, X. Sun and J. Qiu, *Nano Energy*, 2017, **41**, 66.
27 Y. Lu, Q. Zhao, N. Zhang, K. Lei, F. Li and J. Chen, *Adv. Funct. Mater.*, 2016, **26**, 911.
28 L.-Y. Jing, G. Lian, F. Niu, J. Yang, Q.-L. Wang, D.-L. Cui, C.-P. Wong and X.-Z. Liu, *Nano Energy*, 2018, **51**, 546.
29 Y.-P. Liu, X.-Y. He, D. Hanlon, A. Harvey, J.-N. Coleman and Y.-G. Li, *ACS Nano*, 2016, **10**, 8821.
30 R. Wang, S. Wang, Y. Zhang, D. Jin, X. Tao and L. Zhang, *Nanoscale*, 2018, **10**, 11165.
31 L. Fang, Y. Y. Shu, A. Wang and T. Zhang, *J. Phys. Chem. C*, 2007, **111**, 2401.

32 M.-S. Park, G. K. Veerasubramani, R. Thangavel, Y.-S. Lee and D.-W. Kim, *ChemElectroChem*, 2019, **6**, 1.
33 Y. Sun, X. Hu, J.-C. Yu, Q. Li, L. Yuan, W. Zhang and Y. Huang, *Energy Environ. Sci.*, 2011, **4**, 2870.
34 T. Weber, J.-C. Muijsers, J. H. M. C. van Wolput, C. P. J. Verhagen and J.-W. Niemantsverdriet, *J. Phys. Chem.*, 1996, **100**, 14144.
35 X.-W. Lou and H.-C. Zeng, *Chem. Mater.*, 2002, **14**, 4781.
36 E. Lalik, W. I. F. David, P. Barnes and J. F. C. Turner, *J. Phys. Chem. B*, 2001, **105**, 9153.
37 K. Krishnamoorthy, G. K. Veerasubramani, S. Radhakrishnan and S.-J. Kim, *Mater. Res. Bull.*, 2014, **50**, 499.
38 K.-D. Rasamani, F. Alimohammadi and Y. Sun, *Mater. Today*, 2017, **20**, 83.
39 J. Xie, J. Zhang, S. Li, F. Grote, X. Zhang, H. Zhang, R. Wang, Y. Lei, B. Pan and Y. Xie, *J. Am. Chem. Soc.*, 2013, **135**, 17881.
40 K. Krishnamoorthy, G. K. Veerasubramani, P. Pazhamalai and S.-J. Kim, *Electrochim. Acta*, 2016, **190**, 305.
41 F.-H. Zheng, Q.-C. Pan, C.-H. Yang, X.-H. Xiong, X. Ou, R.-Z. Hu, Y. Chen and M. L. Liu, *Chem.–Eur. J.*, 2017, **23**, 5051.
42 Q.-C. Pan, F.-H. Zhang, Y.-N. Wu, X. Ou, C.-H. Yang, X.-H. Xiong and M.-L. Liu, *J. Mater. Chem. A*, 2018, **6**, 592.
43 X.-Q. Xie, Z.-M. Ao, D.-W. Su, J.-Q. Zhang and G. X. Wang, *Adv. Funct. Mater.*, 2015, **25**, 1393.
44 G. K. Veerasubramani, Y. Subramanian, M.-S. Park, G. Nagaraju, B. Senthilkumar, Y.-S. Lee and D.-W. Kim, *J. Mater. Chem. A*, 2018, **6**, 20056.
45 J. Qiu, Z. Zhang, Q. Li, Y. Li, X. Wu, C. Qi and Q. Qian, *J. Mater. Chem. A*, 2016, **4**, 13296.
46 L. David, R. Bhandavat and G. Singh, *ACS Nano*, 2014, **8**, 1759.
47 Y. Xiao, S.-H. Lee and Y.-K. Sun, *Adv. Energy Mater.*, 2017, **7**, 1601329.
48 Z. Hu, L. Wang, K. Zhang, J. Wang, F. Cheng, Z. Tao and J. Chen, *Angew. Chem., Int. Ed.*, 2014, **53**, 12794.
49 V. Augustyn, J. Come, M.-A. Lowe, J.-W. Kim, P.-L. Taberna, S.-H. Tolbert, H.-D. Abruna, P. Simon and B. Dunn, *Nat. Mater.*, 2013, **12**, 518.
50 Y. Subramaniam, M.-S. Park, G. K. Veerasubramani, Y.-S. Lee and D.-W. Kim, *Mater. Chem. Phys.*, 2019, **224**, 129.
51 C. Lai, Y. Y. Dou, X. Li and X. P. Gao, *J. Power Sources*, 2010, **195**, 3676.
52 T. Brezesinski, J. Wang, S.-H. Tolbert and B. Dunn, *Nat. Mater.*, 2010, **9**, 146.
53 G. K. Veerasubramani, M.-S. Park, J.-Y. Choi, Y.-S. Lee, S.-J. Kim and D.-W. Kim, *ACS Sustainable Chem. Eng.*, 2019, **7**, 5921.

